Pyrolytic Graphite Sheet: a New Adsorption Substrate for Superfluid Thin Films

Sachiko Nakamura[a,*], Daisuke Miyafuji[b], Takenori Fujii[a], Tomohiro Matsui[b], Hiroshi Fukuyama[a,b,*]

[a] *Cryogenic Research Center, The University of Tokyo, 2-11-16, Yayoi, Bunkyo-ku, Tokyo 133-0032, Japan*
[b] *Department of Physics, The University of Tokyo, 7-3-1, Hongo, Bunkyo-ku, Tokyo 133-0033, Japan*

arXiv:1704.03204v1 [cond-mat.mtrl-sci] 11 Apr 2017

Abstract

We have made comprehensive measurements of physical properties of uncompressed pyrolytic graphite sheet (uPGS), a mass-produced thin graphite sheet with various thicknesses between 10 and 100 μm. The measured properties include morphology, crystalline structure, impurities and defects, gas adsorption characteristics, and electrical and thermal transport ones. We employed a variety of measuring techniques such as imagings with optical microscope, SEM and STM, X-ray diffraction, Raman spectroscopy, adsorption isotherm, and so on. PGS has smooth and atomically-flat external surfaces with high crystallinity and high thermal conductivity. Although the specific surface area (≤ 0.1 m^2/g) is rather small, the thinnest uPGS of 10 μm thick was found to be suitable for a substrate in torsional oscillator and thermal flow experiments to search for the proposed supersolidity in the second layer of ^{4}He adsorbed on graphite at $T \leq 1$ K.

Keywords: graphite, adsorption, helium, monolayer, superfluidity, supersolidity

1. Introduction

Helium (He) films adsorbed on graphite substrate are experimental realization of correlated two-dimensional quantum systems. With increasing the density, the films grow layer by layer and each layer forms a variety of quantum phases such as gas, liquid, commensurate solid, and incommensurate solid. The commensurability here is with respect to the periodic potential of underlayers like graphite surface or helium monolayer. Very recently, a new class of matter, quantum liquid crystal (QLC), where spatial symmetry is partially broken keeping finite fluidity even at $T = 0$, has been proposed in the second monolayer of ^{4}He as an additional member to them [1]. Moreover, superfluidity has been detected below 400 mK in previous torsional oscillator experiments for this QLC phase [2–4]. So this could be a *supersolid*, a novel state of matter in nature which researchers have been searching for so long [5]. However, the detection efficiency in those studies are rather poor (only 2–6%) because of complicated structure and discontinuity of the surface of substrate, Grafoil, they used. In addition, liquid or amorphous ^{4}He trapped in heterogeneities of the substrate might be responsible for the detected superfluid responses.

Grafoil is a flexible exfoliated graphite sheet [6]. It consists of small natural graphite crystals which are first powdered, then exfoliated at high temperature, and finally rolled under high pressure. This substrate has widely been used as the most standard one in the past experiments for helium thin films [7, 8]. The advantage of the material is its large specific surface area (≈ 20 m^2/g). On the other hand, it has a rather small single crystallite size (= 10–20 nm), giving rise to size limited effects such as smearing of specific heat anomalies at phase transitions [9].

ZYX [10] is an excellent alternative to Grafoil because it has a moderate specific surface area (≈ 2 m^2/g) and much larger single crystallite size (=100–200 nm). It is synthesized by exfoliation of HOPG, highly oriented pyrolytic graphite, and then by recompressing into a density around 2 g/cm^3. Not often, but ZYX has been used in high precision heat capacity measurements both for the first layer [9, 11] and second layer [1] of helium where much more quantitative information on the phase transition and phase stability was obtained.

However, surprisingly enough, ZYX is found to be a less effective substrate than Grafoil in the most recent torsional oscillator experiment [12] in which superfluidity is not detected in films less than three layers. In this paper, we have identified the reason for this failure as deep crevices created by the exfoliation process which are covering the whole surface. Therefore, it is crucial for testing the QLC and supersolid conjecture in the second layer of ^{4}He to find or develop a new graphite substrate with both large enough surface area and less surface irregularities than Grafoil and ZYX.

Here we show results of extensive characterizations of pyrolytic graphite sheet (PGS) [13] which is a candidate substrate for such purposes. PGS is a very thin graphite sheet of 10–100 μm in thickness with a highly-oriented single-crystal-like structure. Note that it is not easy to cut or cleave a HOPG block into many thin pieces of such

*Corresponding author
Email addresses: snakamura@crc.u-tokyo.ac.jp (Sachiko Nakamura), hiroshi@phys.s.u-tokyo.ac.jp (Hiroshi Fukuyama)

thicknesses for torsional oscillator experiments. We make use of external surface instead of internal surface of PGS for helium adsorption unlike the exfoliated graphites. The characterizations include (i) surface morphology observations with optical microscope, scanning electron microscope, and scanning tunneling microscope, (ii) crystallographic observations with X-ray diffraction and Raman scattering, and (iii) physical property measurements of adsorption isotherm, electrical conductivity, and thermal conductivity. We concluded that uncompressed PGS of 10–20 μm thick is capable to detect superfluidity of adsorbed monolayer of ^{4}He below $T = 1$ K.

2. Pyrolytic Graphite Sheet (PGS)

Commercial PGS [13] (hereafter, cPGS) is made first by carbonizing a stack of polymer films of a few μm thick at $T \lesssim 1000$ K, then by graphitizing the resultant foamed carbon precursor at $T \approx 3000$ K, and finally by compression (rubbing) by 30–50% in thickness. Unlike chemical vapor deposition, this is a convenient mass production method for thin graphite sheets of good crystallinity. The previous transmission electron microscopy (TEM) observation [14] show that the cross-sectional structure of a similar kind of graphite is laminar of ultra-thin crystalline graphite layers of 6–7 nm thick which corresponds to 16–20 graphenes. The average lateral size of each layer is considered as 10–100 μm from electron channeling contrast imaging with scanning electron microscope (SEM) [15]. In general, thinner cPGS has higher crystallinity because, in the graphitization process, the liberated gas can escape more easily and the temperature distribution is more uniform.

The final compression procedure makes cPGS flexible like a paper so as to be useful in practical applications. However, it may break the lateral crystalline structure in a large scale spoiling its applicability to superflow experiments of adsorbed helium films. This was eventually the case as is described latter. Therefore, in this work, we studied physical properties of uncompressed PGS (hereafter, uPGS) which is produced by exactly the same method as cPGS except the absence of the final compression. Mechanically uPGS is brittle and inflexible. Thus it is generally difficult to cut it into desired size without, for example, a precise punch designed for cutting thin metal films [16].

Nominal thicknesses of uPGS studied here are 10, 17, 25, and 100 μm. We denote them as uPGS-10μm, for example, in the following. Their actual thicknesses measured by micrometer are 19±2, 29.7±0.6, 56±3, and 145±4 μm, respectively. For comparison we also studied properties of cPGS-10μm whose measured thickness is 13±2 μm.

3. Morphology

We first checked morphology of cleaved surfaces of Grafoil and ZYX in a relatively macroscopic scale with an optical microscope [17]. As shown in Fig. 1(a), the surface of Grafoil is quite irregular with a mosaic structure consisting of plates of random size. As shown in Fig. 1(b), the surface of ZYX is much more uniform. However, we found that it is fully covered by a network of deep crevices of 1–10 μm long. This crevice structure is caused definitely by the exfoliation process of this product, and it should prevent simply connected superflow in ^{4}He films adsorbed on it. So this must be the reason for the failure of the previous torsional oscillator experiment using ZYX [12].

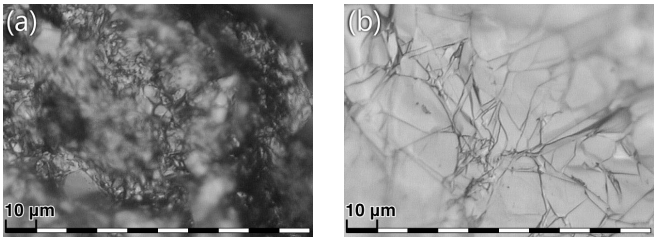

Figure 1: Optical microscope image of a cleaved surface of (a) Grafoil and (b) ZYX.

Secondary electron imaging with a scanning electron microscope (SEM) [18] is more sensitive to a tiny height variation of surface than optical microscope imaging. Figures 2(a) and (b) are such images of cleaved surfaces of Grafoil and ZYX. They have a piled-up structure consisting of 1–20 μm wide patches with sharp edges. This structure presumably reflects small graphite flakes, a raw material, in the case of Grafoil and a trace of rupture in exfoliation in the case of ZYX. In any case, the structure will largely reduce the connectivity of superflow in adsorbed ^{4}He thin films as was actually found in the previous torsional oscillator experiments [2–4].

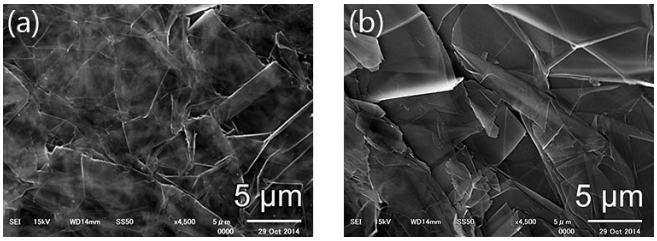

Figure 2: Secondary electron SEM image of a cleaved surface of (a) Grafoil and (b) ZYX.

Next we examined morphology of a cleaved surface of uPGS-10μm with optical microscope as shown in Fig. 3(a). It is completely different from those of Grafoil and ZYX. The surface is quite smooth with a winkle (or wavy) structure of the length scale of 20–40 μm without any crevices. On the other hand, in the case of cPGS-10μm (Fig. 3(b)), the surface is little more complicated with small structures as well as sharp creases which must be created by the final compression process. Thus uPGS should be more suitable for superflow experiments than cPGS.

Figure 4(a) is a secondary electron SEM image of a cleaved surface of uPGS-17μm. It was very difficult to ob-

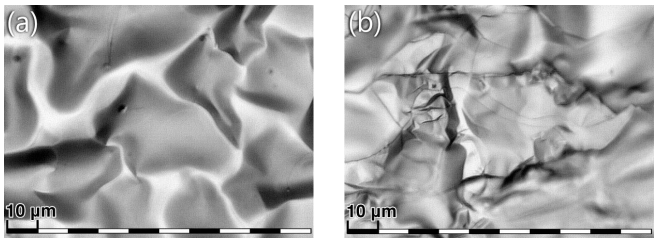

Figure 3: Optical microscope image of a cleaved surface of (a)uPGS-10μm and (b) cPGS-10μm.

tain enough contrast indicating a quite smooth surface. A vaguely seen structure of the length scale of 50–100 μm here is an alternative looking of the winkles. The situation is somewhat different for uPGS-100μm as shown in Fig. 4(b) where the structure is much sharper and smaller. The image contrast is also much higher. Apparently, thicker uPGSs have less uniformity compared to thinner ones because gas is probably more difficult to escape during the carbonization process in the former case.

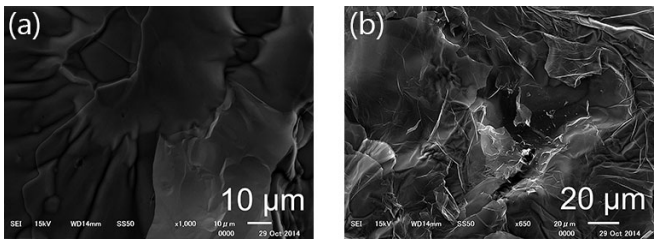

Figure 4: Secondary electron SEM image of a cleaved surface of (a)uPGS-17μm and (b)uPGS-100μm.

Internal morphology was investigated by cross sectional SEM imaging of a fragment torn from a small uPGS piece using a vise (see Figs. 5(a) and (b)). The images show lamination of wavy layers of sub-μm thick. A similar layer structure has also been observed in the previous TEM studies [14]. Note that each layer is an order of magnitude thinner than raw polymer films before carbonization. In uPGS-17μm the layers are rather densely packed, while in uPGS-100μm they are loosely packed with large interlayer spaces which may or may not connect to the outside.

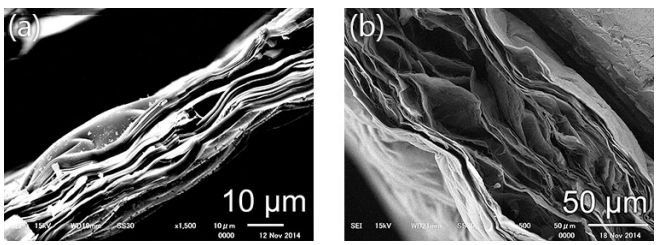

Figure 5: Secondary electron SEM image of a cross section of (a)uPGS-17μm and (b)uPGS-100μm.

A cleaved surface of uPGS-17μm was investigated with a scanning tunneling microscope (STM) [19] at room temperature in the air. As shown in Fig. 6, an atomic resolution of the honeycomb structure of the graphite basal plane was obtained almost everywhere indicating very flat surface. Note that, in STM imaging of a surface of graphite with the normal AB (Bernal) stacking, only carbon atoms belonging to one of two sublattices in topmost graphene are visible. That is why a triangular lattice rather than a honeycomb lattice is observed in Fig. 6. Besides the wavy structure of the order of 1 μm, which is the smaller scale structure seen by SEM, we observed monoatomic height steps separated by about 100 nm (see Fig. 7). These steps may contribute to flow impedance in experiments for superfluid helium films to some extent.

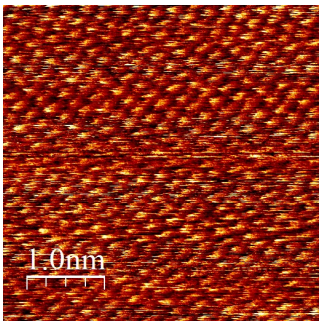

Figure 6: (a) STM topography image of a cleaved surface of uPGS-17μm. A $Pt_{0.8}Ir_{0.2}$ tip was used. The bias voltage V and tunneling current I are 500 mV and 1.01 nA, respectively.

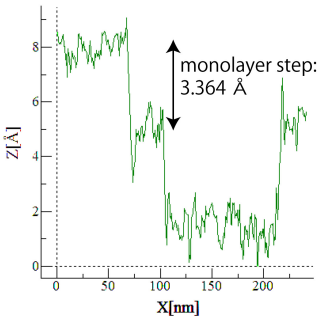

Figure 7: (b) Line profile of an STM image of a cleaved surface of uPGS-17μm.

4. Crystalline Structure and Defects

Out-of-plane X-ray diffraction was measured for uPGS-17μm with a powder X-ray diffractometer [20] using Cu Kα_1 emission. The uPGS sample of 10 × 10 mm^2 was glued onto a glass holder with GE 7031 varnish. Sharp diffraction peaks from graphite are observed indicating that PGS is made purely of graphite crystals. Interplanar spacing d_{002} is determined as 0.33583(7) nm from peaks indexed as (002), (004), and (006) using Nelson-Riley function [21]. From the rocking curve of the (002) peak at 2θ = 26.346 deg, the mosaic angle spread is determined as 8.2±0.1 deg. The mosaic angle spread (= 10±3 deg) roughly estimated from the cross sectional SEM image of Fig. 5(a) is consistent with this value. In-plane X-ray diffraction was also carried out (the data not shown here). The sample was a stack of 29 uPGS-100μm sheets (13×5 mm^2 each) fixed with epoxy glue (Stycast 1266) each other. In addition to the peaks from regular spacing between graphene layers such as (002), those from in-plane honeycomb lattice such as (110), and peaks indicative of three-dimensional graphite lattice indexed as (101), (102), (103), and (112), are observed. d_{002} is determined as 0.33592(6) nm from (002), (004), and (006) peaks, and the in-plane lattice parameter a is determined as 0.2463 nm

from (100) and (110) peaks. All these diffraction results agree very well with the previous study for pyrographite films [22].

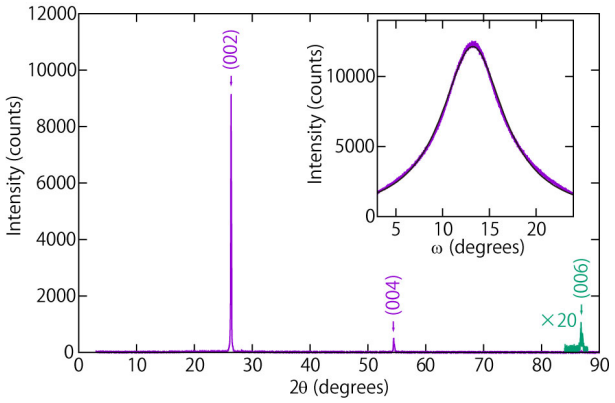

Figure 8: Out-of-plane X-ray diffraction spectrum for uPGS-17μm. (Inset) Rocking curve of (002) peak at $2\theta = 26.346$ deg where the FWHM is 8.2 deg.

Raman spectra of cleaved surfaces of uPGS of 17, 25, and 100 μm thick were measured at 532 nm using a laser Raman microscope [23] with a fixed exposure time of 8 seconds. For comparison, cleaved surfaces of HOPG, ZYX, and Grafoil were also measured. The most intensive features in Raman spectroscopy for graphite are G ($\approx$1580 cm^{-1}) and G' ($\approx$2710 cm^{-1}) peaks. The relative intensity of G peak to G' one, I(G)/I(G'), and the full width at half maximum (FWHM) of G' peak are good representatives of the number n of graphene layers for $n \lesssim 6$ [24]. All measured I(G)/I(G') values (see Table 1) and FWHM values of G' band ($\approx$ 60 cm^{-1}: not shown in the table) for uPGS are similar to those of other graphites, which confirms that they are thick enough graphites. D band is known to appear if the surface contains edges or defects where the three-fold symmetry of honeycomb lattice is broken [25]. The D band signal was not detected in uPGS and HOPG within experimental errors indicating high crystallinity with immeasurably small amounts of domains and defects [26]. On the other hand, for non-cleaved top surfaces of uPGSs, we observed small dust grains distributing over the surface where I(G)/I(G') and I(D)/I(G) values are much smaller and much larger than those at cleaved surfaces, respectively. As discussed in Appendix in detail, they are identified as protruded graphite clusters of multi-layer height ($n < 5$) covering only a few percents of the total surface. The grains were not observed at cleaved surfaces at all.

5. Adsorption Isotherm Measurement

It is crucial to know gas adsorption characteristics of uPGS to apply the material to a substrate for experiments of adsorbed thin films. For this purpose, we made adsorption isotherm measurements of nitrogen molecules (N_2) at $T = 77$ K for uPGS of 100 μm and 17 μm thick.

Table 1: Intensity ratios of I(D)/I(G) and I(G)/I(G') in Raman spectra for various graphite materials. All the surfaces were cleaved before the measurements.

material	nominal thickness	I(D)/I(G)	I(G)/I(G')
uPGS	100 μm	$< 10^{-3}$	3.2(1)
	25 μm	$< 10^{-3}$	3.1(1)
	17 μm	$< 10^{-3}$	3.1(1)
HOPG	—	$< 10^{-3}$	3.3(2)
ZYX	—	0.003(2)	3.2(1)
Grafoil	130 μm	0.015(4)	3.3(1)
	250 μm	0.033(4)	3.3(1)

The uPGS-17μm sample is a stack of 204 uPGS sheets whose total weight is 1.14 g. The size of each sheet is 0.7×2.1 cm^2. The sheets were *loosely* packed into a $2.2 \times 2.2 \times 0.7$ cm^3 open box made of a thin copper plate. They were baked at 700 °C in vacuum ($< 10^{-5}$ torr) and then quickly installed in a vacuum chamber (sample cell). The nominal surface area ($S_{\rm nom}$) calculated from the size and number of sheets is 600 cm^2 without taking account of the wavy surface morphology and intra-sheet space.

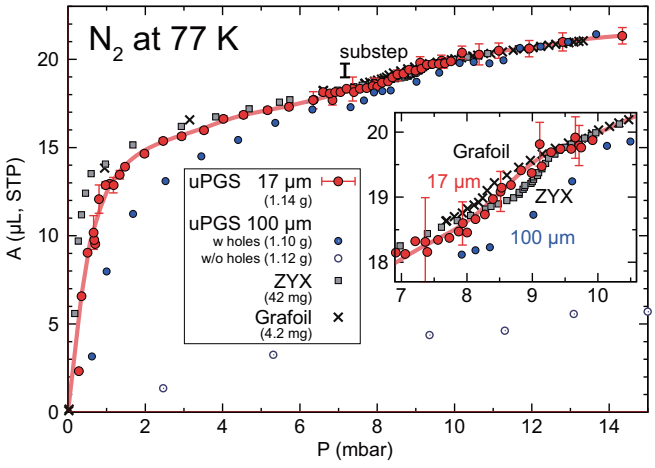

Figure 9: Adsorption isotherms of N_2 at $T = 77$ K for uPGS of 17 μm (closed circles) and 100 μm (smaller circles) thick, ZYX (Ref.[27]; squares), and Grafoil (Ref.[28]; crosses). All the $A_{\rm ad}$ data are scaled to that of uPGS-17μm at $P \geq 12$ mbar. The data for uPGS-17μm were reproducible among several independent measurements. (Inset) Substeps associated with formation of the $\sqrt{3} \times \sqrt{3}$ commensurate phase of 6.37 nm^{-2}.

Measured pressure isotherm data for uPGS-17μm are shown in Fig. 9 by the closed circles. Before discussing the result, let us first explain some technical details to perform this kind of measurement for bulk materials with tiny specific surface area (s), i.e., surface area per unit weight, because it is much more difficult than the measurement on porous or powder materials. In Fig. 9 the

vertical quantity ($A_{\rm ad}$) is an amount of N_2 adsorbed on the surface, and the horizontal one (P) is the equilibrium gas pressure measured by a capacitive pressure gauge [29] located at room temperature. Here an amount of gaseous N_2 existing in an open volume (or dead volume) $V_{\rm dead}$ in the cell has already been subtracted from the raw data. $V_{\rm dead}$ ($\sim$ 20 cm^3) was measured precisely with ^{4}He gas, which is not adsorbed on the surface at 77 K, in a separate run. The apparent (skeletal) density of the sample can be determined by measuring $V_{\rm dead}$ with and without the sample. The thermal transpiration effect [30] in the pressure measurement was directly measured for empty cell with N_2 and was taken into account at $P \leq$2 mbar.

As shown in Fig. 9, the data for uPGS-17μm agree reasonably well with those of ZYX (squares) [27] and Grafoil (crosses) [28]. The "substep" feature (vertical bar) for the $\sqrt{3}\times\sqrt{3}$ commensurate phase ($\rho = 6.37$ atoms/nm^2) formation [31] is clearly seen near $P = 9$ mbar. This also insures that the surface has nearly the perfect graphite structure in atomic scale. The surface area (S) determined from the upper bound of the substep is 830 cm^2. This value is larger than $S_{\rm nom}$ by 40%, which is attributable to the existence of non-negligible internal surface area. Note that the wavy morphology of outer surface increases $S_{\rm nom}$ only by $\approx$ 3%. The apparent density of the uPGS-17μm sample is estimated as 1.76$\pm$0.03 g/cm^3, while that of bulk graphite is 2.26 g/cm^3, indicating the existence of internal void space not accessible for N_2 molecules from outside.

Next, we show a result of uPGS-100μm. The measurement was much more difficult than the 17μm thick sample due to its much smaller $S_{\rm nom}$. The sample is a stack of 36 uPGS-100μm sheets whose total weight is 1.10 g. The size of each sheet is 2 $\times$ 2 cm^2. To reduce time constant for pressure equilibrium, 26–32 holes of 0.5 mm diameter had been drilled through the sheets in equal spacing of 3.2 mm. After baking at 400°C in vacuum ($< 10^{-5}$ torr), the sheets were *tightly* packed into a 2.1 $\times$ 2.1$\times$0.7 cm^3 pocket in the sample cell. $S_{\rm nom}$ is about 220 cm^2. The data for uPGS-100μm also show a substep structure but at a slightly higher pressure (see Fig. 9). This pressure shift corresponds to a small T variation of +0.3 K [32]. From the substep we determined S as 970$\pm$20 cm^2 which is 4 times larger than $S_{\rm nom}$. In addition, the apparent density (= 1.20 g/cm^3) is much smaller than the bulk value. Thus, compared to uPGS-17μm, the 100 μm-thick sample has a much larger inaccessible intra- and/or inter-sheet void volume. In the figure, also plotted by open circles are the data for uPGS-100μm before making the drill holes. In this case S is smaller by more than a factor of 4 than those after drilling indicating a more inaccessible volume. The results of the adsorption isotherm measurements are summarized in Table 2.

6. Electrical Resistivity Measurement

We made in-plane ($\rho_{||}$) and out-of-plane ($\rho_\perp$) electrical resistivity measurements for uPGS samples of four different thicknesses, i.e., 10, 17, 25, and 100 μm, in a temperature range between 2 and 300 K. They were carried out by the 4-terminal method using the AC transport and resistance options of Physical Properties Measurement System (PPMS) of Quantum Design, Inc. The typical sample size is 0.5 $\times$ 9 mm^2 for the $\rho_{||}$ measurement and 3 $\times$ 3 mm^2 for the $\rho_\perp$ one. Gold lead wires of 50 μm in diameter were glued to the samples with rubber-based carbon paste [33] which is strongly adhesive to graphite.

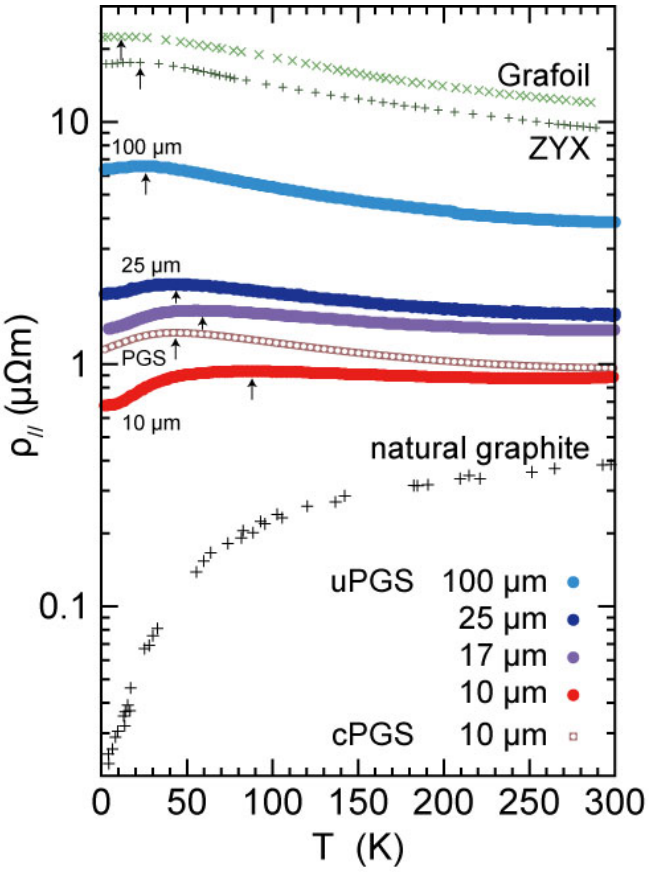

Figure 10: Temperature dependencies of $\rho_{||}$ of uPGS with various thicknesses (solid circles) and cPGS-10μm (open circles). The arrows indicate peak temperatures. Data of Grafoil, ZYX [28] and natural graphite [34] are also plotted.

Results of the $\rho_{||}$ measurement are shown in Fig. 10. $\rho_{||}$ values of the uPGS samples are in between those of exfoliated graphites (Grafoil and ZYX) and natural graphite. Importantly, thinner uPGS has lower $\rho_{||}$ in order of thickness. This is consistent with the fact that thinner uPGS has better crystallinity. Note that the variation of $\rho_{||}$ with thickness, 3–5 times, is much larger than the variation of density, twice at most.

For exfoliated graphite it is known that there are two different conduction mechanisms. One is the metallic one which dominates low temperature behavior of $\rho_{||}$ and $\rho_\perp$, and the other is the variable range hopping (VRH) one which dominates high temperature behavior [28, 35]. As a result, there exists a peak temperature ($T_{\rm peak}$) in ρ vs. T around 20 K that separates the two behaviors as shown in

Table 2: Summary of adsorption isotherm measurements for uPGS.

nominal thickness	drill holes	baking	$S_{\rm nom}$ (cm^2)	weight (g)	density (g/cm^3)	S (cm^2)	s (m^2/g)
17 μm	—	700°C, 1h	600±2	1.14	1.76	830	0.073
100 μm	—	—	286.7±0.2	1.12	0.81	220	0.020
100 μm	ϕ1 × 30	400°C, 1h	271.1±0.2	1.10	1.20	970	0.088

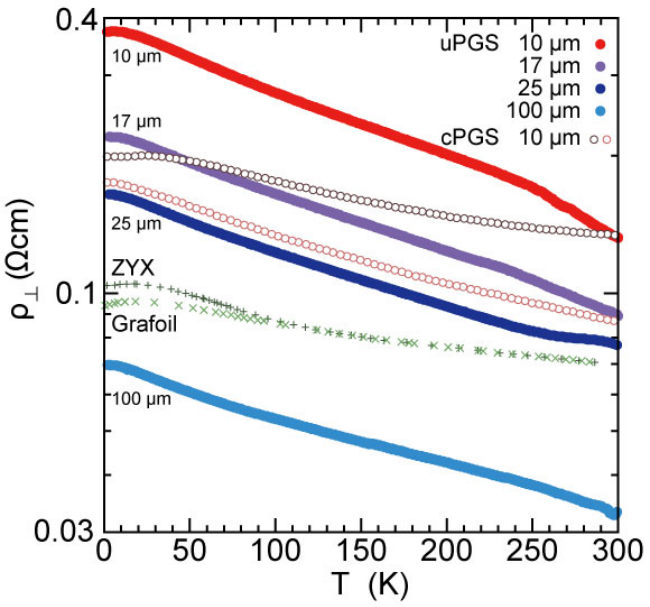

Figure 11: Temperature dependencies of $\rho_\perp$ of uPGS with various thicknesses (solid circles) and cPGS-10μm (open circles). Data of Grafoil and ZYX are also plotted [28].

Fig. 10. We observed a similar T dependence for uPGS but with higher $T_{\rm peak}$ (indicated by the arrows in the figure) again in order of thickness. As the thickness decreases, the T dependence of $\rho_{||}$ becomes weaker above $T_{\rm peak}$ and stronger below $T_{\rm peak}$. The measured in-plane conductivity $\sigma_{||}$ ($=1/\rho_{||}(T)$) is well described by the following equation below 150 K:

$$\sigma = \frac{1}{\rho_0 + AT} + \sigma_0^{\rm h} \exp\left(-\frac{T_0}{T}\right)^{\alpha}, \qquad (1)$$

where the first term corresponds to the metallic channel ($\sigma_{\rm metal}$) and the second term to the hopping one. Within the VRH model,

$$T_0 = \lambda^3 / D_{\rm F} k_{\rm B}, \qquad (2)$$
$$\alpha = 1/(d+1), \qquad (3)$$

for hopping in d spatial dimensions. Here λ and $D_{\rm F}$ are the decay length of the localized electronic wave function and the density of states at the fermi energy, respectively. The hopping is presumably between neighboring microcrystallites across domain boundaries. Thinner uPGS has longer λ and smaller ρ_0, the residual resistivity, presumably because of larger microcrystalline size and less crystalline defects. This explains the thickness dependence of $T_{\rm peak}$. It is noted that in our analysis α is a fitting parameter unlike the previous works [28, 35]. The fittings give $\alpha \approx 1.0$, which corresponds to a simple Arrhenius type conduction, for all the samples.

Figure 11 shows results of the $\rho_\perp$ measurement. Again $\rho_\perp$ at a fixed temperature varies in order of thickness but with an opposite sign to $\rho_{||}$, i.e., thinner uPGS has larger $\rho_\perp$. This is naturally understood as follows. Graphite is a layered material with very weak interlayer coupling based on the van der Waals interaction. Thus the anisotropy of resistivity ($\eta = \rho_\perp/\rho_{||} > 10^2$ [34, 36]) is so large that it can easily be reduced if the system has a mosaic angle spread or the wavy laminar structure. The $\rho_\perp$ data below 150 K can also be well fitted by Eq. 1 with $\alpha \approx 0.5$, nearly one dimensional hopping, being consistent with the above argument on large η. If we make the same analysis for the previously reported $\rho_\perp$ data of ZYX and Grafoil in Refs. [28, 35], we obtain a similar result ($\alpha = 0.42$), although in those papers the data were analyzed assuming $\alpha = 0.25$ (three dimensional hopping). We note that uPGS of any thickness has a kink in the T dependence of $\rho_\perp$ at $T \approx 250$ K above which the dependence changes randomly in every thermal cycle. This results in a ±5% difference in resistivity at 300 K. The mechanism behind this curious behavior is not known at present, but the morphology of uPGS with many microscopic inaccessible voids could be changed either by thermal expansion or by desorption/adsorption of gas confined in the voids in every cooling and warming cycle. The T dependence of $\rho_\perp$ is excellently reproducible at $T < 250$ K for uPGS and in the whole T range we studied for cPGS.

The final compression to produce cPGS provides quantitatively different T dependencies of electrical conductance from those of uPGS. The open symbols in Figs. 10 and 11 are results of $\rho_{||}$ and $\rho_\perp$ measurements for cPGS-10μm. Compared to uPGS-10μm, the $\rho_{||}$ value at room temperature is only slightly larger. However, it has a steeper variation down to $T_{\rm peak}$, and $T_{\rm peak}$ itself is lower. Therefore, the overall T dependence of cPGS-10μm is rather similar to those of the exfoliated graphites. This would be a result of mixing between $\rho_{||}$ and $\rho_\perp$ caused by the compression. The same is true for $\rho_\perp$ where the cPGS-10μm samples have much weaker T variations. This is again similar to the behavior of exfoliated graphite. It should be noted that the magnitude of $\rho_\perp$ and sometimes even its T dependence differ largely sample to sample in the case of cPGS, thus two different samples are shown in Fig. 11, presumably because the compression damages the laminar structure. Also, α values scatter to a large extent from 0.26 to 0.42.

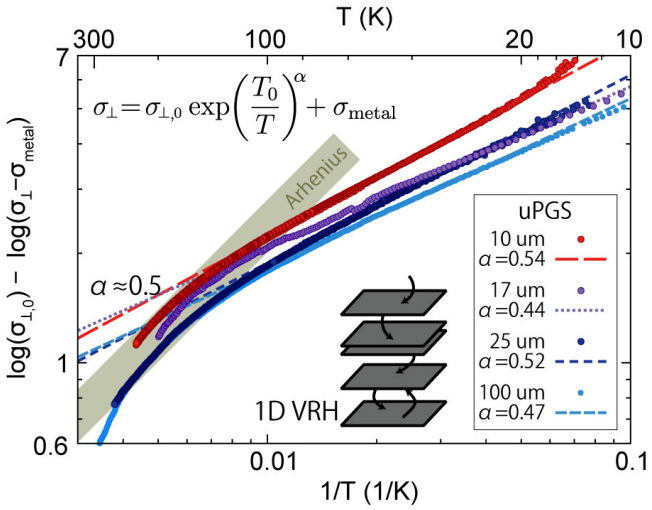

Figure 12: Temperature dependencies of the out-of plane conductivity $\alpha_\perp$ of various uPGS samples plotted as logarithm of $\alpha_\perp$ vs. $1/T$. This plot demonstrates that α is close to 1/2 rather than 1/4 expected from the 3D VRH model (see main text). The inset is a schematic diagram of the one dimensional inter-plane hopping.

7. Thermal Conductivity Measurement

To prepare uniform film samples of helium in terms of temperature and density, it is important to use adsorption substrates with high thermal conductivity (κ) at low temperature. Usually, for metallic samples, κ can be estimated from the electrical resistivity ρ, which can more easily be measured, through the Wiedemann-Franz (WF) law [37]. However, in the case of semimetal such as graphite, the WF law underestimates κ by several orders of magnitude at temperatures where the thermal conduction by phonons plays an important role [38]. Thus we have measured in-plane κ of uPGS-10μm directly using Thermal Transport option of PPMS. The sample of 7 mm wide and 8 mm long was glued on 4 gold-plated copper electrodes with silver paste. The electrodes are fixed to a thin rectangular support rod made of Stycast 2850FT ($2 \times 0.5 \times 8\,\mathrm{mm}^3$). The thermal conductivity of the support rod is negligibly small at temperatures above 50 K and is less than half of the total conductivity at lower temperatures.

In Fig. 13, measured κ data of uPGS-10μm (closed circles) are shown with those of natural graphite (open circles) [39], HOPG (solid line) [38], ZYX [40], and Grafoil [40]. Although the T dependence of κ of uPGS-10μm is remarkably similar to those of ZYX and Grafoil in the whole T range between 2 and 300 K, it has more than one order of magnitude higher conductivity than the exfoliated graphites. This is a great advantage of this material indicating the longer mean-free path of phonons and thus the higher crystallinity. A peak in $\kappa(T)$ around 150 K corresponds to the onset of Umklapp scattering. It is in between the peak temperature ($T_{\mathrm{peak}} = 100\,\mathrm{K}$) of natural graphite and HOPG and those ($T_{\mathrm{peak}} \approx 200\,\mathrm{K}$) of ZYX and Grafoil. At $30 \le T \le 100\,\mathrm{K}$, the T dependence is $\kappa \propto T^{2.01(2)}$ as expected from two-dimensional phonon conductivity. It turns to $\kappa \propto T^{2.55(2)}$ at lower temperatures ($2 \le T \le 30\,\mathrm{K}$) where the conductivity is lower than that of natural graphite by a factor of 4–10.

In Fig. 13, we also plotted thermal conductivity estimated from the WF law (κ_{WF}: broken lines). All of them are much lower than the measured ones. In addition, T dependencies of κ_{WF} are quite different from the measured ones. Nevertheless, it is interesting to note that the ratios ($= \kappa/\kappa_{\mathrm{WF}}$) are rather similar within a factor of 8 among the different graphites in the whole T range. In this sense, the WF law still provides a useful "rough" estimation for κ from an electrical resistivity measurement for a variety of graphite materials. We thus believe in that uPGS-10μm has the highest κ among other PGSs judging from its lowest $\rho_{||}$ (see Fig. 10).

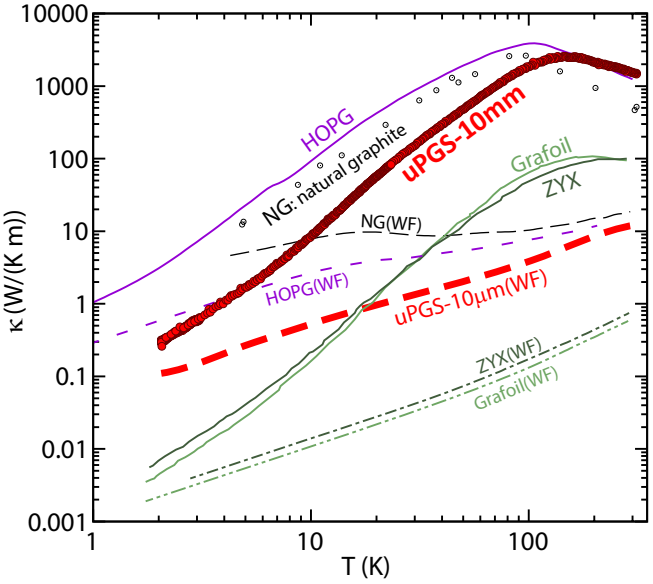

Figure 13: Temperature dependencies of in-plane thermal conductivity κ of uPGS-10μm, HOPG [38], natural graphite [39], Grafoil [40], and ZYX [40]. Thermal conductivity estimated from electric conductivity using the Wiedemann-Franz (WF) law is indicated as dashed lines for each specimen [28, 34, 41].

8. Feasibility Studies of Experiments on Superfluid Thin Films Using uPGS

In this section, we show feasibility studies of detection of superfluidity in monolayer of ^{4}He adsorbed on a PGS substrate at temperatures below 1 K by making use of torsional oscillator and thermal flow techniques. For these studies, among other types, uPGS-10-μm was chosen as a substrate mainly because of its largest specific surface area and the highest in-plane thermal conductivity.

Torsional oscillator experiment

The substrate for torsional oscillator experiment will consist of a stack of 1000 uPGS-10-μm disks of 20 mm in diameter and silver foils of 2 μm in thickness and 8 mm

in diameter. They will alternately be piled up and be diffusively bonded at 600 K under pressure to make them a rigid single piece. Then it will be tightly packed into a container made of magnesium alloy of 20 mm in height and 1 mm wall thickness. An estimated total surface area of uPGS is 0.53 m^2. The silver foils are used to make proper gaps between the uPGS disks, and to assist the thermal conductance and the rigidity of the uPGS disks. The adsorption potential of silver for helium is 3 times less than that of graphite [42]. Thus the second layer of ^{4}He adsorbed on uPGS should be in equilibrium with a submonolayer ^{4}He adsorbed on silver which will not show superfluidity being tightly bound to the surface.

The superfluidity will be detected as a resonance frequency shift (Δf) of the torsional oscillator due to a change of the moment of inertia (I). I values of the ^{4}He-QLC phase (7.5 atoms/nm^{-2} [1]), the uPGS discs, and the container are 1.8×10^{-12} kg·m^2, 3.1×10^{-7} kg·m^2, and 2.3×10^{-7} kg·m^2, respectively. Note that I of the silver foils is negligibly small compared to that of the He film. Thus Δf is expected to be ≈ 2.9 mHz, while an accuracy of Δf is typically ≈ 0.02 mHz [12]. Therefore, even if the detection efficiency of the uPGS surface is of the order of 0.1, the superfluidity should clearly be detected.

Thermal flow experiment

An abrupt increase of the thermal conductance along a ^{4}He thin film provides an alternative evidence for superfluid onset of the film with increasing the coverage at a fixed T or decreasing T at a fixed coverage. For this type of experiment, the substrate crystallinity should be as high as possible not to reduce the superflow, and the substrate thickness should be as thin as possible not to shunt the temperature gradient by substrate itself when the film is in the normal state. The previous experiment [43] using a ZYX wafer of $25 \times 25 \times 5$ mm^3 was successful to detect superfluid onset of a ^{4}He thin film of three atomic layers at $T = 1.0$ K with increasing the coverage. uPGS-10-μm should potentially be more advantageous for this experiment than ZYX because of its much better crystallinity as described in this paper.

Next we recall another previous experiment [44] where a thin HOPG leaf ($2 \times 14 \times 0.1$ mm^3) was successfully used to detect third sound propagation of a ^{4}He thin film of three atomic layers adsorbed on it at $T = 1.0$ K. The third sound is a temperature wave (or equivalently an entropy wave) characteristic of superfluid thin films. This experiment demonstrates that the thermal transport phenomenon of such a thin superfluid film can be detected not being shunted by the 100 μm-thick graphite substrate. We thus expect that uPGS-10μm will be capable enough to detect superfluid onset of even thinner ^{4}He films in the second layer.

9. Conclusions

We measured physical properties of uPGSs (uncompressed pyrolytic graphite sheets) of various thicknesses between 10 and 100 μm, which are thin graphite sheets suitable for mass production, including morphology, crystal structure and defects, adsorption isotherm, and electrical and thermal conductivities. It was concluded that the thinnest uPGS (uPGS-10-μm) has the smoothest surface, highest crystallinity, highest conductivities, and largest specific surface area. Except its much less flexibility, uPGS has better physical properties than cPGS (commercial pyrolytic graphite sheet), the product obtained by compressing uPGS.

We also made feasibility studies of torsional oscillator experiment and thermal transport measurement to search for the possible superfluidity of the recently proposed quantum liquid crystal phase in the second layer of ^{4}He adsorbed on uPGS-10μm. The results were encouragingly positive. Besides the detection of superfluidity, uPGS will be useful for other applications such as excellent heatsink in a wide temperature range from cryogenic to high temperature, high-conductivity carbon electrode in electrochemistry, new functional materials based on graphite intercalation techniques, etc.

10. Acknowledgements

We are grateful to Yoshiya Sakaguchi, Hiroyuki Hase, and Makoto Nagashima of Automotive & Industrial Systems Company of Panasonic corporation for providing us the uPGS and cPGS samples. We also thank Hideki Sato for his assistance to take the STM image of uPGS.

This work was financially supported by Grant-in-Aid for Scientific Research (B) (Grant No. 15H03684), and Challenging Exploratory Research (Grant No. 15K13398) from JSPS. The laser Raman microscope used in this work was supplied by MERIT program, The University of Tokyo.

References

[1] S. Nakamura, K. Matsui, T. Matsui, H. Fukuyama, Possible quantum liquid crystal phases of helium monolayers, Phys. Rev. B 94 (2016) 180501. doi:10.1103/PhysRevB.94.180501.
URL http://link.aps.org/doi/10.1103/PhysRevB.94.180501

[2] P. A. Crowell, J. D. Reppy, Reentrant superfluidity in ^{4}He films adsorbed on graphite, Phys. Rev. Lett. 70 (1993) 3291–3294. doi:10.1103/PhysRevLett.70.3291.
URL http://link.aps.org/doi/10.1103/PhysRevLett.70.3291

[3] Y. Shibayama, H. Fukuyama, K. Shirahama, Torsional oscillator studies for possible supersolidity in two-dimensional ^{4}He solid, Journal of Physics: Conference Series 150 (3) (2009) 032096.
URL http://stacks.iop.org/1742-6596/150/i=3/a=032096

[4] J. Nyéki, A. Phillis, A. Ho, D. Lee, P. Coleman, J. Parpia, B. Cowan, J. Saunders, Intertwined superfluid and density wave order in two-dimensional ^{4}He, Nature Physics advance online publication.
URL http://dx.doi.org/10.1038/nphys4023

[5] K. R. A. Hazzard, Quantum physics: A solid more fluid than a fluid, Nature 543 (7643) (2017) 47–48.
URL http://dx.doi.org/10.1038/543047a

[6] GrafTech International Ltd. Former Carbon Products Division of Union Carbide (UCAR).

[7] M. Bretz, J. G. Dash, Quasiclassical and quantum degenerate helium monolayers, Phys. Rev. Lett. 26 (1971) 963–965. doi:10.1103/PhysRevLett.26.963.
URL http://link.aps.org/doi/10.1103/PhysRevLett.26.963

[8] M. W. Cole, D. R. Frankl, D. L. Goodstein, Probing the helium-graphite interaction, Rev. Mod. Phys. 53 (1981) 199–210. doi:10.1103/RevModPhys.53.199.
URL http://link.aps.org/doi/10.1103/RevModPhys.53.199

[9] M. Bretz, Ordered helium films on highly uniform graphite — finite-size effects, critical parameters, and the three-state potts model, Phys. Rev. Lett. 38 (1977) 501–505. doi:10.1103/PhysRevLett.38.501.
URL http://link.aps.org/doi/10.1103/PhysRevLett.38.501

[10] GE Advanced Ceramics.

[11] S. Nakamura, K. Matsui, T. Matsui, H. Fukuyama, Preliminary heat capacity and vapor pressure measurements of 2D ^{4}He on ZYX graphite, Journal of Low Temperature Physics 171 (5–6) (2013) 711–717. doi:10.1007/s10909-012-0847-5.
URL http://dx.doi.org/10.1007/s10909-012-0847-5

[12] S. Nakamura, R. Toda, Y. Kubota, M. Kamada, H. Fukuyama, to be published.

[13] Panasonic Corporation, Automotive & Industrial Systems Company.

[14] N. Nishiki, H. Take, M. Murakami, S. Yoshimura, K. Yoshino, Synthesis and characterization of pyrolytic graphite from heat-treated polyimide, IEEJ Transactions on Fundamentals and Materials 123 (11) (2003) 1115–1123, (in Japanese). doi:10.1541/ieejfms.123.1115.
URL http://ci.nii.ac.jp/naid/10012555627/en/

[15] Y. Kaburagi, Preparation of graphite films from aromatic polyimide films and characterization, TANSO 2013 (258) (2013) 216–229, (in Japanese). doi:10.7209/tanso.2013.216.
URL http://ci.nii.ac.jp/naid/10031183877/en/

[16] Handheld punch manufactured by NOGAMIGIKEN CO., LTD.

[17] VH-5000 Digital Microscope manufactured by Keyence Corporation.

[18] JSM-6610LV manufactured by JEOL Ltd.

[19] Specially manufactured by Omicron Vakuumphysik GMBH based on their commercial model MICRO-STM.

[20] RINT powder X-ray diffractomater manufactured by Rigaku Corporation.

[21] J. Nelson, D. Riley, LXXXVI. orientation effect in powder photographs of graphite, The London, Edinburgh, and Dublin Philosophical Magazine and Journal of Science 36 (261) (1945) 711–714. arXiv:http://dx.doi.org/10.1080/14786444508520959, doi:10.1080/14786444508520959.
URL http://dx.doi.org/10.1080/14786444508520959

[22] M. Murakami, K. Watanabe, S. Yoshimura, High-quality pyrographite films, Applied Physics Letters 48 (23) (1986) 1594–1596. arXiv:http://dx.doi.org/10.1063/1.96827, doi:10.1063/1.96827.
URL http://dx.doi.org/10.1063/1.96827

[23] RAMAN-FM-UTM manufactured by Nanophoton Corporation.

[24] A. C. Ferrari, J. C. Meyer, V. Scardaci, C. Casiraghi, M. Lazzeri, F. Mauri, S. Piscanec, D. Jiang, K. S. Novoselov, S. Roth, A. K. Geim, Raman spectrum of graphene and graphene layers, Phys. Rev. Lett. 97 (2006) 187401. doi:10.1103/PhysRevLett.97.187401.
URL http://link.aps.org/doi/10.1103/PhysRevLett.97.187401

[25] S. Reich, C. Thomsen, Raman spectroscopy of graphite, Philosophical Transactions of the Royal Society of London A: Mathematical, Physical and Engineering Sciences 362 (1824) (2004) 2271–2288. doi:10.1098/rsta.2004.1454.

[26] H. Wilhelm, M. Lelaurain, E. McRae, B. Humbert, Raman spectroscopic studies on well-defined carbonaceous materials of strong two-dimensional character, Journal of Applied Physics 84 (12) (1998) 6552–6558. arXiv:http://dx.doi.org/10.1063/1.369027, doi:10.1063/1.369027.
URL http://dx.doi.org/10.1063/1.369027

[27] S. Nakamura, K. Matsui, T. Matsui, H. Fukuyama, New heat-capacity measurements of the possible order-disorder transition in the 4/7-phase of 2D helium, Journal of Physics: Conference Series 400 (3) (2012) 032061.
URL http://stacks.iop.org/1742-6596/400/i=3/a=032061

[28] Y. Niimi, S. Murakawa, Y. Matsumoto, H. Kambara, H. Fukuyama, Characterization of ZYX exfoliated graphite for studies of monolayer ^{3}He below 1 mK, Review of Scientific Instruments 74 (10) (2003) 4448–4452. doi:10.1063/1.1606540.
URL http://link.aip.org/link/?RSI/74/4448/1

[29] Setra Systems, Inc.

[30] T. Takaishi, Y. Sensui, Thermal transpiration effect of hydrogen, rare gases and methane, Transactions of the Faraday Society 59 (1963) 2503–2514.

[31] J. K. Kjems, L. Passell, H. Taub, J. G. Dash, A. D. Novaco, Neutron scattering study of nitrogen adsorbed on basal-plane-oriented graphite, Phys. Rev. B 13 (1976) 1446–1462. doi:10.1103/PhysRevB.13.1446.
URL http://link.aps.org/doi/10.1103/PhysRevB.13.1446

[32] J. Piper, J. A. Morrison, C. Peters, Y. Ozaki, Heats and entropies of adsorption of N_2 on grafoil at 79.3 K, J. Chem. Soc., Faraday Trans. 1 79 (1983) 2863–2874. doi:10.1039/F19837902863.
URL http://dx.doi.org/10.1039/F19837902863

[33] Varniphite UCC-320 by Nippon Graphite Industries, Co., Ltd.

[34] W. Primak, L. H. Fuchs, Electrical conductivities of natural graphite crystals, Phys. Rev. 95 (1954) 22–30. doi:10.1103/PhysRev.95.22.
URL http://link.aps.org/doi/10.1103/PhysRev.95.22

[35] C. Uher, Thermopower of exfoliated graphites between 1.7 and 300 K, Phys. Rev. B 25 (1982) 4167–4172. doi:10.1103/PhysRevB.25.4167.
URL http://link.aps.org/doi/10.1103/PhysRevB.25.4167

[36] G. E. Washburn, Der einfluß der magnetisierung auf den gleichstromwiderstand des graphits nach der hauptachse, Annalen der Physik 353 (18) (1915) 236–250. doi:10.1002/andp.19153531806.
URL http://dx.doi.org/10.1002/andp.19153531806

[37] R. Franz, G. Wiedemann, Ueber die wärme-leitungsfähigkeit der metalle, Annalen der Physik 165 (8) (1853) 497–531. doi:10.1002/andp.18531650802.
URL http://dx.doi.org/10.1002/andp.18531650802

[38] D. T. Morelli, C. Uher, Thermal conductivity and thermopower of graphite at very low temperatures, Phys. Rev. B 31 (1985) 6721–6725. doi:10.1103/PhysRevB.31.6721.
URL http://link.aps.org/doi/10.1103/PhysRevB.31.6721

[39] A. W. Smith, Low-temperature thermal conductivity of a canadian natural graphite, Phys. Rev. 95 (1954) 1095–1096. doi:10.1103/PhysRev.95.1095.
URL http://link.aps.org/doi/10.1103/PhysRev.95.1095

[40] C. Uher, Thermal conductivity of several exfoliated graphites from 2 K to 300 K, Cryogenics 20 (8) (1980) 445–447. doi:http://dx.doi.org/10.1016/0011-2275(80)90075-2.
URL http://www.sciencedirect.com/science/article/pii/0011227580900752

[41] D. T. Morelli, C. Uher, T^2 dependence of the in-plane resistivity of graphite at very low temperatures, Phys. Rev. B 30 (1984) 1080–1082. doi:10.1103/PhysRevB.30.1080.
URL http://link.aps.org/doi/10.1103/PhysRevB.30.1080

[42] E. Cheng, M. W. Cole, W. F. Saam, J. Treiner, Phase transitions in multilayer helium films, Phys. Rev. B 46 (1992) 13967–13982. doi:10.1103/PhysRevB.46.13967.
URL http://link.aps.org/doi/10.1103/PhysRevB.46.13967

[43] S. Polanco, M. Bretz, Thermal resistivity of layered ^{4}He films on ZYX graphite below 2 K, Surface Science 94 (1) (1980) 1–15. doi:http://dx.doi.org/10.1016/0039-6028(80)90152-1.
URL http://www.sciencedirect.com/science/article/pii/

0039602880901521
[44] J. Maynard, M. Chan, Third sound on HOPG preface, Physica B+C 109 (1982) 2090 – 2092. doi:http://dx.doi.org/10.1016/0378-4363(82)90585-X.
URL http://www.sciencedirect.com/science/article/pii/037843638290585X
[45] W. Bao, J. Wan, X. Han, X. Cai, H. Zhu, D. Kim, D. Ma, Y. Xu, J. N. Munday, H. D. Drew, M. S. Fuhrer, L. Hu, Approaching the limits of transparency and conductivity in graphitic materials through lithium intercalation, Nature Communications 5 (2014) 4224.

Appendix A. Dust Grains on Top Surface of PGS

In both uPGS and cPGS, regardless of thickness, we found many tiny grains distributing inhomogeneously all over the wavy top surfaces before cleavage as shown in the optical microscope image of Fig. A.14. The grains are optically black.

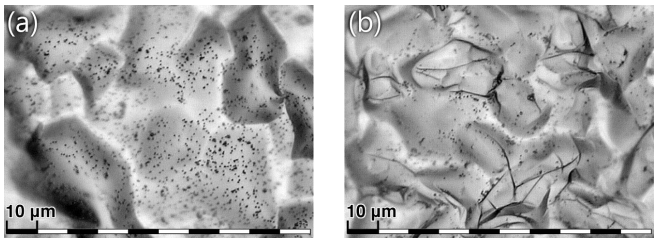

Figure A.14: Optical microscope image of a top surface of uncleaved (a)uPGS-10μm and (b)cPGS-10μm.

The grain size determined from secondary electron microscope imaging is from 0.2 to 2 μm in diameter (see Fig. A.15(a)). They are protruded from the surface judging from the back scattered SEM imaging of Fig. A.15(b). Clearly, the grains are stuck only on top surfaces, since they are completely absent on cleaved surfaces as were already shown in Figs. 3 and 4. They cannot be removed by neither baking at 700 °C in vacuum ($< 10^{-5}$ torr) nor washing with solvents such as aceton, ethanol, isopropanol, water, and water with surface-active agent.

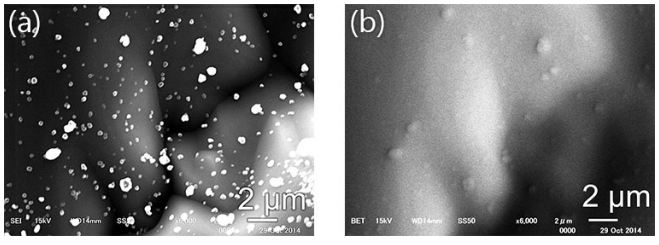

Figure A.15: SEM images of a top surface of uncleaved uPGS-17μm observed with (a)secondary electrons and (b)back scattered electrons.

The energy-dispersive X-ray spectroscopy, which is sensitive to boron and heavier elements, detected no traces other than carbon and oxygen on the top surfaces with the grains.

Table A.3: Intensity ratios of I(D)/I(G) and I(G)/I(G') in Raman spectra for uncleaved top surfaces of uPGS.

material	nominal thickness	I(D)/I(G)	I(G)/I(G')
uPGS	100 μm	0.028(5)	1.3–3.3
	25 μm	0.018(11)	0.3–3.0
	17 μm	0.013(5)	0.3–3.2

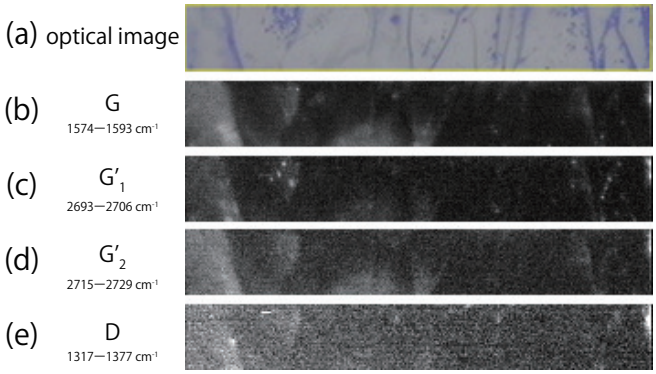

Figure A.16: (a)Optical image and (b)–(e)Raman intensity maps corresponding to G, G_1', G_2', and D peaks at the top surface of uncleaved uPGS-100μm. Brighter contrast means stronger Raman intensity in the range of wavenumber indicated on left. Width and height are $8.7\times68.2\,\mu\mathrm{m}^2$ for each.

Raman spectra gave us many insights about the origin of the surface grains. First of all, as shown in Table A.3, spatially averaged I(D)/I(G) and I(G)/I(G') values are quite different form those of cleaved surfaces (see Table 1). We observed relatively large intensities of G_1' band, a lower wavenumber component of G' peak at $\approx 2700\,\mathrm{cm}^{-1}$, at the grains in Raman spectra mapping as shown in Fig. A.16(c) where some of the grains found in the optical image (Fig. A.16(a)) are clearly seen as bright spots. The G' peak at such grains is more symmetrical (red dots in Fig. A.17) compared to that at clean graphite surface (blue dots), which is characteristic of a few layer thick graphene [24]. A spatial variation of the D band intensity (Fig. A.16(e)) is more or less similar to those of G and G'$_2$ bands (Figs. A.16(b,d)), where G'$_2$ is a higher wavenumber component of G' peak, reflecting the surface wimples not the distribution of the surface grains. As was mentioned in the main text, D band intensity was not observed at cleaved surfaces so that such defects locate only around the top surface. They may be associated with defects located below the top surface by several tens graphene layer [45].

From all these results, we conclude that the surface grain is a stack of graphite microcrystallites consisting of relatively small numbers of graphene layers. The grains can be removed by cleaving the surface with scotch tape, and possibly by other methods like hydrogen plasma etching.

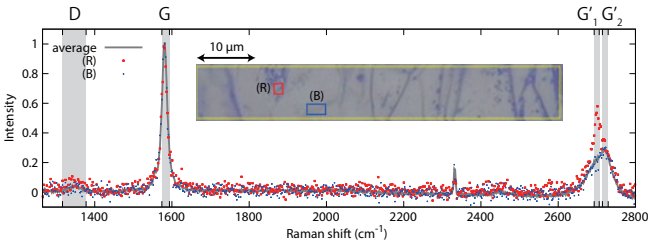

Figure A.17: Raman spectra taken at two different regions of the top surface of uncleaved uPGS-100μm. Those regions are indicated by the red (with grain) and blue squares (without grain) in the inset which is the same image as Fig. A.16(a). The intensity is normalized by the peak height of G peak. The background intensity of a glass substrate used to fix the uPGS sample has already been subtracted from the data shown here.